Sensitivity-based optimization for the design of a grating interferometer for clinical X-ray phase contrast mammography

Arboleda, Carolina ; Wang, Zhentian ; Koehler, Thomas ; Martens, Gerhard ; Van Stevendaal, Udo ; Bartels, Matthias ; Villanueva-Perez, Pablo ; Roessl, Ewald ; Stampanoni, Marco

Abstract: An X-ray grating interferometer (GI) suitable for clinical mammography must comply with quite strict dose, scanning time and geometry limitations, while being able to detect tumors, microcalcifications and other abnormalities. Such a design task is not straightforward, since obtaining optimal phase-contrast and dark-field signals with clinically compatible doses and geometrical constraints is remarkably challenging. In this work, we present a wave propagation based optimization that uses the phase and dark-field sensitivities as figures of merit. This method was used to calculate the optimal interferometer designs for a commercial mammography setup. Its accuracy was validated by measuring the visibility of polycarbonate samples of different thicknesses on a Talbot-Lau interferometer installed on this device and considering some of the most common grating imperfections to be able to reproduce the experimental values. The optimization method outcomes indicate that small grating pitches are required to boost sensitivity in such a constrained setup and that there is a different optimal scenario for each signal type.

DOI: https://doi.org/10.1364/oe.25.006349

Research Article | Vol. 25, No. 6 | 20 Mar 2017 | OPTICS EXPRESS 6349

Optics EXPRESS

Sensitivity-based optimization for the design of a grating interferometer for clinical X-ray phase contrast mammography

CAROLINA ARBOLEDA,[1,2,*] ZHENTIAN WANG,[1,2] THOMAS KOEHLER,[3] GERHARD MARTENS,[3] UDO VAN STEVENDAAL,[3] MATTHIAS BARTELS,[3] PABLO VILLANUEVA-PEREZ,[1,2] EWALD ROESSL,[3] AND MARCO STAMPANONI [1,2]

[1]*Paul Scherrer Institute, 5232 Villigen, Switzerland*
[2]*ETH Zurich, 8092 Zurich, Switzerland*
[3]*Philips Research Laboratories, D-22335 Hamburg, Germany*
[*]*carolina.arboleda@psi.ch*

Abstract: An X-ray grating interferometer (GI) suitable for clinical mammography must comply with quite strict dose, scanning time and geometry limitations, while being able to detect tumors, microcalcifications and other abnormalities. Such a design task is not straightforward, since obtaining optimal phase-contrast and dark-field signals with clinically compatible doses and geometrical constraints is remarkably challenging. In this work, we present a wave propagation based optimization that uses the phase and dark-field sensitivities as figures of merit. This method was used to calculate the optimal interferometer designs for a commercial mammography setup. Its accuracy was validated by measuring the visibility of polycarbonate samples of different thicknesses on a Talbot-Lau interferometer installed on this device and considering some of the most common grating imperfections to be able to reproduce the experimental values. The optimization method outcomes indicate that small grating pitches are required to boost sensitivity in such a constrained setup and that there is a different optimal scenario for each signal type.

OCIS codes: (170.3830) Mammography; (110.7440) X-ray imaging; (080.2740) Geometric optical design; (070.7345) Wave propagation; (050.1950) Diffraction gratings.

References and links

1. S. D. Auweter, J. Herzen, M. Willner, S. Grandl, K. Scherer, F. Bamberg, M.F. Reiser, F. Pfeiffer and, K. Hellerhoff, "X-ray phase-contrast imaging of the breast-advances towards clinical implementation," Br. J. Radiol. **87**, 20130606 (2014).
2. M. Stampanoni, Z. Wang, T. Thüring, C. David, E. Roessl, M.Trippel, R. Kubik-Huch, G. Singer, M. Hohl and N. Hauser, "The First Analysis and Clinical Evaluation of Native Breast Tissue Using Differential Phase-Contrast Mammography," Invest. Radiol. **46(12)**, 801–806 (2011).
3. N. Hauser, Z. Wang, R.A. Kubik-Huch, M. Trippel, G. Singer, M.K. Hohl, E. Roessl, T. Koehler, U. van Stevendaal, N. Wieberneit and M. Stampanoni, "A Study on Mastectomy Samples to Evaluate Breast Imaging Quality and Potential Clinical Relevance of Differential Phase Contrast Mammography," Invest. Radiol. **49(3)**, 131–137 (2013).
4. G. Anton, F. Bayer, M.W. Beckmann, J. Durst, P. A. Fasching, W. Haas, A. Hartmann, T. Michel, G. Pelzer, M. Radicke, C. Rauh, J. Rieger, A. Ritter, R. Schulz-Wendtland, M. Uder, D. L.Wachter, T.Weber, E. Wenkel, and L. Wucherer, "Grating-based dark-field imaging of human breast tissue," Zeitschrift für Medizinische Physik **23(3)**, 228–235 (2013).
5. K. Scherer, L. Birnbacher, M. Chabior, J. Herzen, D. Mayr, and S. Grandl, A. Sztrokay-Gaul, K. Hellerhoff, F. Bamberg and F. Pfeiffer, "Bi-Directional X-Ray Phase-Contrast Mammography," PLoS ONE **9(5)**, e93502 (2014).
6. K. Scherer, K. Willer, L. Gromann, L. Birnbacher, E. Braig, S. Grandl, A. SztrÃşkay-Gaul, J. Herzen, D. Mayr,K. Hellerhoff and F. Pfeiffer, "Toward clinically compatible phase-contrast mammography," PLoS ONE **10(6)**, e0130776 (2015).
7. P.R. Munro, K. Ignatyev, R.D. Speller, and A. Olivo, "Design of a novel phase contrast x-ray imaging system for mammography," Phys. Med. Biol. **55**, 4169–4185 (2010).
8. A. Olivo, S. Gkoumas, M. Endrizzi, C. K. Hagen, M. B. Szafraniec, and P. C. Diemoz, "Low-dose phase contrast mammography with conventional x-ray sources," Med. Phys. **40(9)**, 090701 (2013).
9. E. Roessl, H. Daerr, T. Koehler, G. Martens, and U. van Stevendaal, "Clinical boundary conditions for grating-based differential phase-contrast mammography," Philos. Trans. R. Soc. London, Ser. A **372(2010)**, 20130033 (2014).

#285536 https://doi.org/10.1364/OE.25.006349
Journal © 2017 Received 26 Jan 2017; revised 7 Mar 2017; accepted 7 Mar 2017; published 10 Mar 2017

Optics EXPRESS

10. T. Koehler, H. Daerr, G. Martens, N. Kuhn, S. Loescher, U. van Stevendaal, and E. Roessl, "Slit-scanning differential x-ray phase-contrast mammography: Proof-of-concept experimental studies," Med. Phys. **42(4)**, 1959–1965 (2015).
11. T. Weitkamp, A. Diaz, C. David, F. Pfeiffer, M. Stampanoni, P. Cloetens, and E. Ziegler, "X-ray phase imaging with a grating interferometer," Opt. Express **13**, 6296–6304 (2005).
12. C. Kottler, F. Pfeiffer, O. Bunk, C. Grunzweig, and C. David, "Grating interferometer based scanning setup for hard x-ray phase contrast imaging," Rev. Sci. Instrum. **78**, 043710 (2007)
13. F. Pfeiffer, T. Weitkamp, O. Bunk and C. David, "Phase retrieval and differential phase-contrast imaging with low-brilliance X-ray sources," Nat. Phys. **2(4)**, 258–261 (2006).
14. P. Modregger, B. Pinzer, T. Thüring, S. Rutishauser, C. David, and M. Stampanoni, "Sensitivity of X-ray grating interferometry," Opt. Express **19(19)**, 18324–18338 (2011).
15. V. Revol, C. Kottler, R. Kaufmann, U. Straumann, and C. Urban, "Noise analysis of grating-based X-ray differential phase contrast imaging," Rev. Sci. Instrum. **81(7)**, 0737091–4 (2010).
16. T. Thüring, Compact X-ray grating interferometry for phase and dark-field computed tomography in the diagnostic energy range, ETH PhD thesis (2013).
17. D. Atwood, *Soft X-Rays and Extreme Ultraviolet Radiation, Principles and Applications* (Cambridge University, 2007).
18. T. Michel, J. Rieger, G. Anton, F. Bayer, M.W Beckmann, J. Durst, P. A. Fasching, W. Haas, A. Hartmann, G. Pelzer, M. Radicke, C. Rauh, A. Ritter, P. Sievers, R. Schulz-Wendtland, M. Uder, D.L. Wachter, T. Weber, E. Wenkel, and A. Zang, "On a dark-field signal generated by micrometer-sized calcifications in phase-contrast mammography," Phys. Med. Biol. **58(8)**, 2713–2732 (2013).
19. Z. Wang, N. Hauser, G. Singer, M. Trippel, R. Kubik-Huch, C. Schneider, and M. Stampanoni, "Non-invasive classification of microcalcifications with phase-contrast X-ray mammography," Nat. Commun. **5**, 1–9 (2014).
20. Z. Wang, N. Hauser, R. Kubik-Huch, F. D'Isidoro, and M. Stampanoni, " Quantitative volumetric breast density estimation using phase contrast mammography," Phys. Med. Biol. **60**, 4123–4135 (2015).
21. S. K. Lynch, V. Pai, J. Auxier, A.F. Stein, E.C. Bennett, C.K. Kemble, X. Xiao, W. Lee, N.Y. Morgan, and H.H. Wen, "Interpretation of dark-field contrast and particle-size selectivity in grating interferometers," Appl. Opt. **50(22)**, 4310–4319 (2011).
22. W. Yashiro, Y. Terui, K. Kawabata, and A. Momose, "On the origin of visibility contrast in x-ray Talbot interferometry," Opt. Express **18(16)**, 16890–16901(2010).
23. M. Strobl, "General solution for quantitative dark-field contrast imaging with grating interferometers," Sci. Rep. **4**, 72431 (2014).
24. M. Fernandez, H. Suhonen, J. KeyrilÃd'inen, A. Bravin, S. Fiedler, M.L. Karjalainen-Lindsberg, M. Leidenius, K. von Smitten, and P. Suortti, "USAXS and SAXS from cancer-bearing breast tissue samples," Eur. J. Radiology **68S**, S89 (2008).
25. Z. Wang, K. Kang, Z. Huang and Z. Chen, "Quantitative grating-based x-ray dark-field computed tomography," Appl. Phys. Lett. **95(9)**, 0941051 (2009).
26. C. Arboleda, Z. Wang Z and M. Stampanoni, "Tilted-grating approach for scanning-mode X-ray phase contrast imaging," Opt. Express **22(13)**, 15447–15458 (2014).
27. J. Boone, T. Fewell, and R. Jennings, "Molybdenum, rhodium, and tungsten anode spectral models using interpolating polynomials with application to mammography," Med. Phys. **24(12)**, 1863–1874 (1997).
28. M. Aslund, B. Cederström, M. Lundqvist, and M. Danielsson, "Physical characterization of a scanning photon counting digital mammography system based on Si-strip detectors," Med. Phys. **34(6)**, 1918–1925 (2007).
29. T. Thüring and M. Stampanoni, "Performance and optimization of X-ray grating interferometry," Phil. Trans. Royal Soc. A **372(2010)**, 20130027 (2014).
30. H. Ding and S. Molloi, "Quantification of breast density with spectral mammography based on a scanned multi-slit photon-counting detector: a feasibility study," Phys. Med. Biol. **57**, 4719–4738 (2012).
31. K. Erhard, E. Fredenberg, H. Homann, and E. Roessl, "Spectral lesion characterization on a photon-counting mammography system," Proc. SPIE Medical Imaging **9033** (2014).
32. H. Johansson, M. von Tiedemann, K. Erhard, H. Heese, H. Ding, S. Molloi, and E. Fredenberg, "Volumetric breast-density measurement using photon-counting spectral mammography," submitted to Med. Phys. (2016)
33. M. J. Berger, J. H. Hubbell, S. M. Seltzer, J. Chang, J. S. Coursey, R. Sukumar, D. S. Zucker, and K. Olsen, *XCOM: Photon Cross Section Database* (version 1.5) (National Institute of Standards and Technology, 1990).
34. F. Pfeiffer, O. Bunk, C. Schulze-Briese, A. Diaz, T. Weitkamp, C. David, J. van der Veen, I. Vartanyants, and I. Robinson, "Shearing interferometer for quantifying the coherence of hard x-ray beams," Phys. Rev. Lett. **94(16)**, 1648011–4 (2005).
35. N. Perry, M. Broeders, C. de Wolf, S. Toernberg, R. Holland, and L. von Karsa L, *European Guidelines for Quality Assurance in Breast Cancer Screening and Diagnosis*, 4th ed. (European communities, 2006).
36. T. Donath, M. Chabior, F. Pfeiffer, O. Bunk, E. Reznikova, J. Mohr, E. Hempel, S. Popescu, M. Hoheisel, M. Schuster, J. Baumann, and C. David, "Inverse geometry for grating-based x-ray phase-contrast imaging," J. Appl. Phys. **106**, 0547031 (2009).
37. L. Gromann, D. Beque, K. Scherer, K. Willer, L. Birnbacher, M. Willner, J. Herzen, S. Grandl, K. Hellerhoff, J. Sperl, F. Pfeiffer, and C. Cozzini, "Low-dose, phase-contrast mammography with high signal-to-noise ratio," Biomed. Opt. Express **7**, 381–391 (2016).

Optics EXPRESS

1. Introduction

The contribution that X-ray grating based phase-contrast imaging can make to mammography has been investigated by several research groups in the last few years [1]. Stampanoni et al [2] measured native mastectomy samples on a Talbot-Lau grating interferometer (GI) and demonstrated that the differential phase-contrast and dark-field signals provided complementary information to the conventional attenuation signal. Later on, Hauser [3] conducted a two-section, prospective independent reader study with six international, expert breast radiologists, who evaluated both conventional and phase-contrast mammograms of fresh mastectomy samples of 33 patients with invasive cancer. The results of the comparison between the outcomes of both methods revealed that phase-contrast mammography was able to provide images with superior quality, increased sharpness, lesion delineation and microcalcification visibility, and clearer delimitation of the anatomic components of the specimens. In conclusion, the overall clinically relevant information yielded by this new technique was judged to be superior.

Likewise, Anton et al [4] investigated six mastectomy samples on a Talbot-Lau interferometer. They demonstrated that it was possible to see important structures on the dark-field images with significantly higher contrast than on the traditional mammogram. In addition, they compared the dark-field signal with histomorphometric images and proved that it correlated with a tumor area containing microcalcifications in the 3-30 μm range. In the meantime, Scherer et al [5] applied a bi-directional phase-contrast mammography approach to a freshly dissected cancerous breast sample and were able to reliably detect tumor structures independently from their orientation within the breast. Later on, Scherer et al [6] presented the first dose-compatible and fast scan-time phase-contrast images of both a freshly dissected cancerous mastectomy sample and a mammographic accreditation phantom.

These outcomes have encouraged the medical and scientific community to pursue the transfer of the phase-contrast technology to the clinics [7,8], which represents a very interesting challenge from the engineering point of view. This step implies the adaptation of the technique to cover a large field of view within a limited exposure time, deliver a radiation dose below 1 mGy per view, be compact in order to comply with the current ergonomic requirements, avoid increasing patient discomfort and yield higher sensitivity to tumors, microcalcifications and other abnormalities [9]. Based on these facts, a straightforward approach would be to design a GI that can fit into an already existing commercial mammography machine.

Following this direction, Koehler et al [10] designed and built a first Talbot order GI with a total length of 55 cm, which they managed to accommodate into a Philips Microdose Mammography setup that features single photon count Silicon microstrip detectors in a scanning geometry able to provide a reduction of the dose. The signal retrieval method was integrated into the scanning motion, so the phase stepping procedure usually employed in conventional GI [11] was avoided. In the scanning approach, a fringe pattern is generated and phase stepping is achieved by moving the object on a path perpendicular to the grating direction [12]. Despite this attempt proved to be able to retrieve absorption, differential phase-contrast and dark-field signals, it yielded a considerably low sensitivity for a mammographic application.

In order to overcome this issue, a wave propagation based optimization focused on maximizing the phase and dark-field sensitivities was developed and used to calculate the optimal GI parameters for the aforementioned Philips device. The predicted values were confronted with actual measurements to verify the accuracy of the algorithm. To be able to reliably reproduce the experimental values, the influence of some of the most common grating fabrication imperfections was assessed as well. Since this setup is designed for a very specific type of sample (i.e. human breasts), a screening database from Soedersjukhuset, Sweden (use of the screening data for general research purposes was done in accordance with local legislation), was used to define the highest occurrence breast, dubbed the target breast in the following, which was utilized for the calculation of our sensitivity metrics.

Optics EXPRESS

2. Methods

2.1. Philips Microdose Mammography setup

The boundary conditions for the design of a GI for the Philips Microdose Mammography are listed in Table 1. Since the X-ray tube focal spot size is 300 μm, a source grating (G0) is necessary to obtain the required spatial coherence [13]. The configuration of this interferometer is sketched in Fig. 1.

Table 1. Philips Microdose Mammography boundary conditions for the GI design.

Parameter	Value
Maximum GI length (cm)	55.6
Peak voltages (kVp)	26, 29, 32, 35 and 38
mAs range	150-1500
Focal spot size (μm)	300
Target material	W
Detector technology	Si-strip photon-counting
Si-strip thickness (mm)	3.6
Pixel pitch (μm)	50
Image matrix (pixels)	4800 × 5200
Field size (cm × cm)	24 × 26

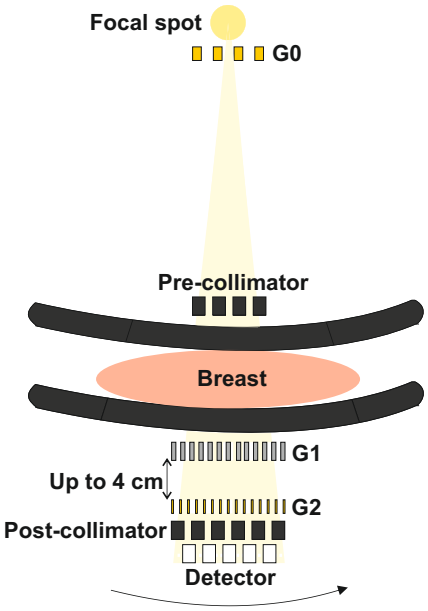

Fig. 1. Sketch of a Talbot-Lau interferometer installed on the Philips Microdose Mammography.

2.2. Figures of merit

2.2.1. Phase sensitivity

The Signal-to-Noise Ratio (SNR) for the phase signal can be expressed as:

Optics EXPRESS

$$SNR_{\phi} = \frac{\phi}{\Delta\phi} = \alpha \frac{2\pi d}{p_2} \frac{1}{\Delta\phi}, \tag{1}$$

where α is the refraction angle, d is the G1-G2 distance and p_2 is the G2 pitch. ϕ corresponds to the differential phase signal and can be defined as follows:

$$\phi = \phi_{background} - \phi_{sample}, \tag{2}$$

Using error propagation and assuming that the sample and background uncertainties are uncorrelated:

$$\Delta\phi = \sqrt{\Delta\phi_{background}{}^2 + \Delta\phi_{sample}{}^2}, \tag{3}$$

Since α is object dependent, our objective will be to minimize the inverse of the remaining factor to optimize the geometry for SNR, i.e:

$$\alpha_{min} = \frac{p_2}{2\pi d} \Delta\phi, \tag{4}$$

which is also known as the minimum detectable refraction angle [14]. Revol et al [15] derived the dependency of $\Delta\phi$ for a photon-counting detector as follows:

$$\Delta^2\phi = \frac{2}{V^{r2} N} \left(1 + \frac{1}{TV^2}\right), \tag{5}$$

where V^r is the background visibility (i.e. calculated from the scan without object), V is the visibility reduction, i.e. $\frac{V^s}{V^r}$, V^s being the object visibility, T is the sample transmission and N is the number of detected photons. The visibility is the contrast of the recorded phase-stepping curve or Moiré fringe [16].

Although the minimum detectable refraction angle can give us an idea of the sensitivity of a GI, what the phase-contrast technology ultimately aims to measure is the electron density (ρ_e) of a material. Therefore, a more adequate way of expressing the phase sensitivity is as the minimum detectable electron density gradient. Having the minimum detectable refraction angle, calculating the latter can be done as follows [17]:

$$\Delta\rho_{e,min} = \frac{2\pi}{r_e \lambda_{\text{eff}}{}^2} \alpha_{min}, \tag{6}$$

where r_e is the classical electron radius and λ_{eff} is a weighted average of the wavelengths of the detected spectrum after the sample, using the spectral visibility as the weighting factor [16].

2.2.2. Dark-field sensitivity

The dark-field signal might represent an important contribution to mammography, since it could help detect microcalcifications that are not visible on absorption [4, 18], distinguish between microcalcification types [19], estimate breast density [20] and potentially differentiate tumors from harmless masses. This signal reflects the small and ultra-small angle scattering (SAXS and USAXS) produced by an object. The USAXS and SAXS signals are generated by the unresolved microscopic structure of the refractive index and cause angular divergence of the incident beam [21]. In grating-based methods, this effect causes a visibility reduction (V) at the detector plane.

The dark-field sensitivity is defined as the corresponding SNR in this paper, i.e:

$$SNR_{df} = \frac{-ln(V)}{\Delta ln(V)}, \tag{7}$$

Optics EXPRESS

whose computation requires the calculation of the visibility reduction produced by the sample. The corresponding dark-field signal can be expressed as follows [21–23]:

$$ln(V) = -\mu_d t = \Sigma t(G(\xi) - 1), \tag{8}$$

where Σ is the macroscopic scattering cross-section, t is the sample thickness, $G(\xi)$ is the real-space correlation function, μ_d is the dark-field extinction coefficient and ξ is the auto-correlation length, i.e:

$$\xi = \frac{\lambda_{\text{eff}} L_s}{p_2}, \tag{9}$$

where L_s is equivalent to the inter-grating distance if the sample is placed on the G1 plane [23]. This means that to be able to predict the visibility reduction produced by breast tissue, we need to derive its corresponding $G(\xi)$.

To achieve this goal, we utilized the data from Fernandez et al [24], who measured the USAXS and SAXS patterns ($I(q)$) from cancer-bearing human breast tissue. To derive $G(\xi)$ from their measurements, we started by regenerating their USAXS curve approximating the first portion as Gaussian and the second one as linear. Afterwards, we fitted this curve to our measurements and eventually took the inverse Fourier transform to get $G(\xi)$ [23].

We measured two formalin-fixed breast specimens with thicknesses of 2.5 cm and 3.6 cm at different ξ and used the data from our fresh mastectomy dataset [3] containing 50 samples. Measurements were conducted on a GI operated with an X-ray tube at 40 kVp. This interferometer has a design energy of 28 keV, a G0 pitch p_0=12.13 μm, G1 pitch p_1=4.80 μm, G2 pitch p_2=3.00 μm and a total length of 110 cm. The auto-correlation length was varied by moving the sample away from G1 and towards G0, and measurements were carried out in the range of auto-correlation lenghts reachable on the Microdose setup. Since data were acquired on a polychromatic setup, the corresponding λ_{eff} was calculated by measuring a PMMA wedge with a 45 degree slope and computing the effective energy from the measured refraction angle.

To calculate the visibility reduction produced by a specimen of a certain thickness, we convoluted the background interference pattern for each λ with the scattering angle distribution $f(x)$, which can be well approximated as a Gaussian:

$$f(x) = \frac{1}{\sigma\sqrt{2\pi}} exp\left[-\frac{1}{2\sigma^2}\left(\frac{x}{d}\right)^2\right], \tag{10}$$

where σ is defined as:

$$\sigma = \sqrt{\frac{\Sigma t(G(\xi) - 1)}{2\pi^2\left(\frac{d}{p_2}\right)^2}}, \tag{11}$$

so that Eq. (8) is satisfied [25].

Afterwards, we performed the usual weighted average using the normalized spectrum to define the corresponding weights to calculate the effective sample interference pattern [16].

To complete the calculation of Eq. (7), $\Delta ln(V)$ can be computed using noise propagation as follows:

$$\Delta ln(V) = \sqrt{\left(\frac{\Delta V^{s2}}{V^{s2}}\right) + \left(\frac{\Delta V^{r2}}{V^{r2}}\right)}, \tag{12}$$

where ΔV^s and ΔV^r correspond to the uncertainties in the sample and background visibilities, respectively, and it was assumed that both uncertainties are uncorrelated. Revol et al [15] found that this noise variance is equivalent to:

Optics EXPRESS

$$\Delta^2 ln(V) = \frac{2}{V^{r2}N}\left(1+\frac{1}{TV^2}\right)+\frac{1}{N}\left(1+\frac{1}{T}\right), \tag{13}$$

It is important to remark that this formula, as well as Eq. (5), only considers the noise contributed by the detector, which is the major source of uncertainty. There can be other possible sources of error, such as those due to mechanical motion (phase stepping or scanning), but these will not be considered in this work, as their contribution is much smaller compared to the detector [15].

It must be mentioned that our derivation of μ_d does not take into account all the potential scatterer shapes and packing distributions that can be encountered in a sample as complex as a human breast. This complexity stems from the fact that there is a very large biological variability, which is extremely challenging to take into account in a complete manner. However, we think that our approach is sufficient for the purpose of this paper, which is to select the optimal GI design scenario for a constrained setup after comparing all the possibilities under the same conditions. Notwithstanding, we are aware of the importance of the absolute visibility and sensitivity values, so we plan to conduct a systematic statistical study on the structures of interest as future work.

2.3. Optimization procedure

A wave propagation code [16, 26] written in Matlab (Mathworks, 2015a) was used to simulate all the potential GI designs for the Philips Microdose setup taking into account the geometric constraints. The total GI length was fixed to 55.6 cm, whereas the inter-grating distance was limited to 4 cm, which is the space available between the breast support and the detector.

The input spectra corresponding to the available peak voltages (see Table 1) were simulated using the algorithm introduced by Boone et al [27]. For designing GI based systems the input spectra accuracy is even more crucial than for X-ray attenuation based setups, since the spectrum shape determines the optimal design energy and the flux absolute values have a major influence in the sensitivity to phase and dark-field changes induced by the sample. The spectra are plotted in Fig. 2 and they already take into account the attenuation produced by the compression paddles (Polycarbonate, 3.66 mm), breast support (Carbon-Fiber-Reinforced Plastic (CFRP), 0.94 mm), gratings and grating wafers. All gratings were assigned a duty cycle of 0.5. The number of photons per pixel for an exposure time of 15 s reported in this figure corresponds to the expected mean photons over the phase stepping curve in the central detector pixel; this value was directly measured on a GI-equipped Philips setup [10]. Since the duty cycle of the simulated G0 was 0.5, whereas that of the experimental setup was 0.4, the flux values were corrected by this ratio. The grating wafers were simulated as Silicon structures with a height of 250 μm. The G1 height is defined by the design energy, while that of the absorption gratings is calculated as to block the highest percentage of photons as possible to optimize interference visibility. Considering current fabrication constraints, which at present limit the aspect ratio of absorption gratings [16], we used a height of 30 μm for the absorption gratings.

Wave propagation was carried out for each 0.5 keV energy bin independently and their contributions were incoherently summed up regarding their relative weight within the normalized spectrum to obtain the resulting phase stepping curve; Poisson noise was added to the latter afterwards. Moreover, the height of the Silicon strip detectors (3.6 mm) [28] was considered as well. A summary of the wave propagation algorithm is presented in a flux diagram in Fig. 3.

A π phase grating was selected for our optimization procedure, since for Talbot orders higher than 1, the use of a $\pi/2$ grating causes a significant visibility drop due to the sign inversion of the fringes for some energies of the input spectrum. This negative effect becomes more relevant as the Talbot order increases, while for Talbot order one it conversely causes a slight visibility improvement, because the sign inversion does not occur in this case [29]. However, the latter improvement is so small that can be disregarded.

Optics EXPRESS

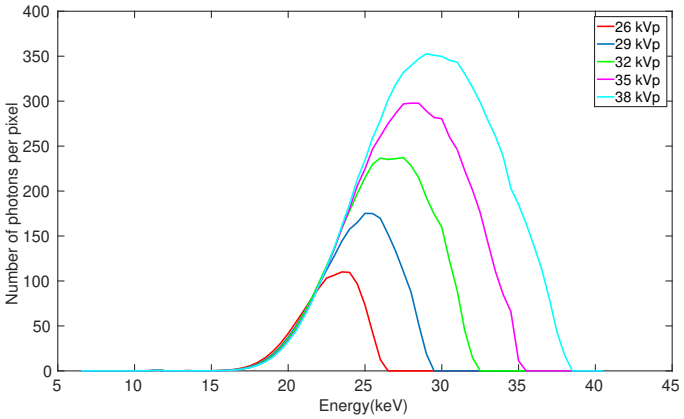

Fig. 2. Simulated spectra after all the GI elements (gratings plus grating wafers) on the beam path assuming 250 μm thick grating wafers for an exposure time of 15 s.

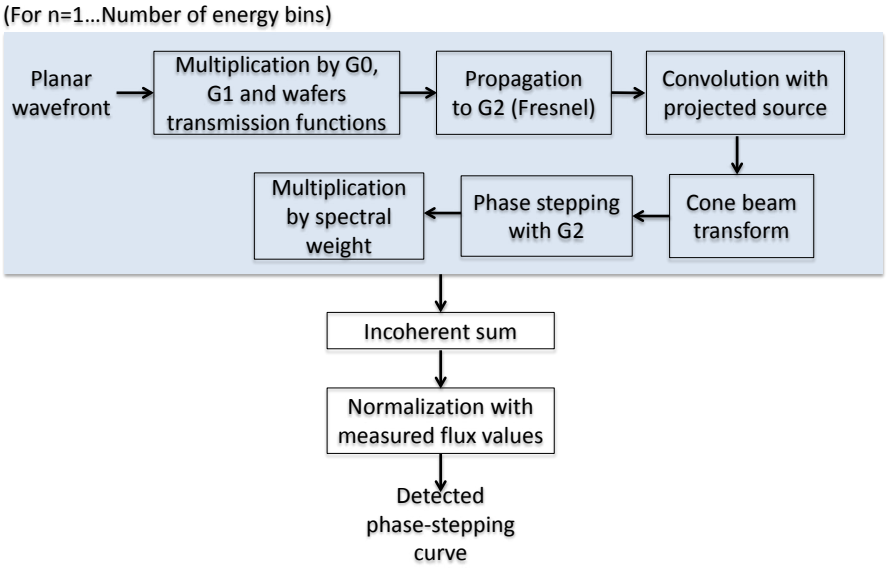

Fig. 3. Summary of the wave propagation simulation.

For the sensitivity metrics computation, a target breast was selected from a screening population comprising 6788 patients that were examined with a Philips Microdose SI system with spectral capabilities, at Soedersjukhuset, Stockholm, Sweden. The highest-occurrence (25.9 %) breast corresponds to an average compression thickness of 7 cm and a glandular density of 18.1 %. The breast density values were calculated with the built-in breast-density measurement tool in the Philips system, for which the spectral image data was decomposed into volumes of glandular and adipose tissue by calibration on tissue-equivalent material [30–32]. The attenuation coefficient of this target breast was calculated using the XCOM photon cross section database of the National Institute of Standards and Technology (NIST) [33], utilizing the breast adipose and glandular tissue compositions defined by the International Commission on Radiation Units and

Optics EXPRESS

Measurements (ICRU) in report 46.

For the calculation of the differential phase and dark-field noise standard deviations, Poisson noise was added to the object and flat phase-stepping curves. Afterwards, Fourier Component Analysis was applied to retrieve the aforementioned signals. The noise addition procedure was repeated until each signal converged to a constant value so that the standard deviation across iterations could be taken as the uncertainty [14]. The resulting standard deviations were further validated by the analytical formulas derived by Revol et al [15].

Due to the low photon fluxes we are working with, the highest flux spectrum was used for our simulations and the design energy range was set to 20-36 keV (Fig. 2). For each design energy, the corresponding p_2 value was calculated, taking into account all the remaining constraints. A summary of the optimization algorithm is presented in Fig. 4.

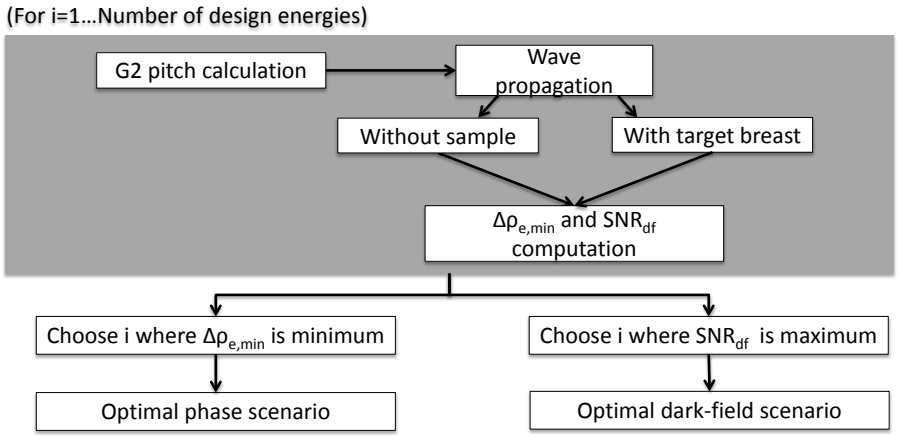

Fig. 4. Summary of the optimization algorithm. An optimal scenario for the phase sensitivity and another for the dark-field SNR are the outcomes of this method.

2.4. Experimental validation

The accuracy of simulations was validated by measuring the visibility reduction produced by Polycarbonate blocks of different thicknesses (0, 20 and 40 mm) on a first order Talbot-Lau interferometer installed in the Philips Microdose using all the available spectra. To be able to reproduce the experimental values, two of the most common grating imperfections, namely in the grating heights and duty cycles (i.e. opening/pitch), were simulated. Only the worst-case scenario values were computed, i.e. having the maximum errors in both parameters and all three gratings at the same time, which according to the fabrication experts are 10% for the height and 20% for the duty cycle. In addition, it was assumed that the scattering produced by the Polycarbonate blocks was negligible.

The GI used for measurements has a total length of 55 cm, a design energy of 25 keV, p_0=27.3 μm, p_1=3.73 μm, p_2=2 μm and an inter-grating distance of 3.75 cm [10]. A source grating with a duty cycle of 0.4 and a thickness of 30 μm was used for these measurements. By verifying the visibility accuracy and using realistic flux values, the uncertainty values ($\Delta ln(V)$ and $\Delta\phi$) get validated as well, since there is an inter-dependency between these metrics, as discussed in section 2.2.

Optics EXPRESS

3. Results and discussion

3.1. Experimental validation

The complete set of results of the experimental visibility validation are presented in Fig. 5. The standard deviation in the predicted values accounts for the variability introduced by the simulated grating height (±10%) and duty cycle (±20%) imperfections. The thickest block (40 mm) visibility could not be measured with the 26 kVp spectrum, because the SNR was not enough to provide a reliable value.

It can be seen that it is hard to predict with full accuracy the visibility due to several experimental factors listed below. In an ideal scenario, this trend depends mainly on two factors: 1) The match between the effective energy of the hardened spectrum and the design energy of the interferometer; the closer this match, the higher the visibility; 2) the scattering produced by the sample, that is highly material-dependent and was assumed to be negligible in this case. However, in practice, other factors also influence this behavior, such as material impurities, grating imperfections and misalignments, as well as mechanical instabilities. For instance, an error in the phase grating height will cause the desired phase shift (either π or $\pi/2$) at an energy different from the design energy so that the predicted variation of the visibility with respect to the input spectrum will differ from the experimental behavior. Therefore, what a simulation tool is able to provide is a range in which the measured visibility values can be expected.

It can be seen on this figure that the experimental values are consistently located at the lowest parts of the simulated bars for the 32 kVp through 38 kVp spectra; however, this is not the case for the lower energy spectra. This can be related to the complex distribution of X-ray emission in the 7 keV-12 keV range for Tungsten, which results in difficulties to simulate low-energy spectra with high accuracy [27]. The fact that the measured values are systematically found at the lowest part of the simulated bars for the higher energy spectra might be due to an underestimation of the real grating fabrication errors.

As explained above, we did not expect to obtain the same measured visibility absolute values with our simulation tool. However, the fact of being able to reproduce the visibility behavior with respect to thickness and spectrum within the most common potential grating fabrication errors is enough to validate the accuracy of our software. In addition, one grating can differ a lot from another in practice, due to the difficulties to have full control over the fabrication process, so there could be local height inhomogeneities (i.e. some grating lines being higher than others) or line distortions (e.g. lines not being straight) which would be hard to account for.

3.2. Derivation of the real-space correlation function for breast tissue

A plot of the derived breast tissue dark-field extinction coefficient μ_d (Eq. (8)) is presented in Fig. 6 including the outcomes of the measurements performed on our setup. The value reported on this figure for the fresh mastectomy database corresponds to the mean of the values presented in Fig. 7.

A good agreement between the data from [24] and ours is observed. The standard deviation in our measurements accounts mainly for the inhomogeneity of the tissue rather than the noise.

It is important to mention that the breast glandular density was not taken into account. For future work, it would be ideal to include this variable into play and of course to increase statistics, because human breast tissue is subject to a significant biological variability. However, we consider that for the purpose of this optimization, this derivation is fair enough.

A fundamental issue for the dark-field signal is the optimization task. Here we are optimizing for breast tissue SNR, but if the diagnostic task is changed, the optimal parameters might change as well. For instance, if the goal of this instrument was to make visible on the dark-field image microcalcifications that cannot be seen in absorption, the goal would become to optimize for microcalcification dark-field contrast-to-noise ratio (CNR). For this purpose, it would be

Optics EXPRESS

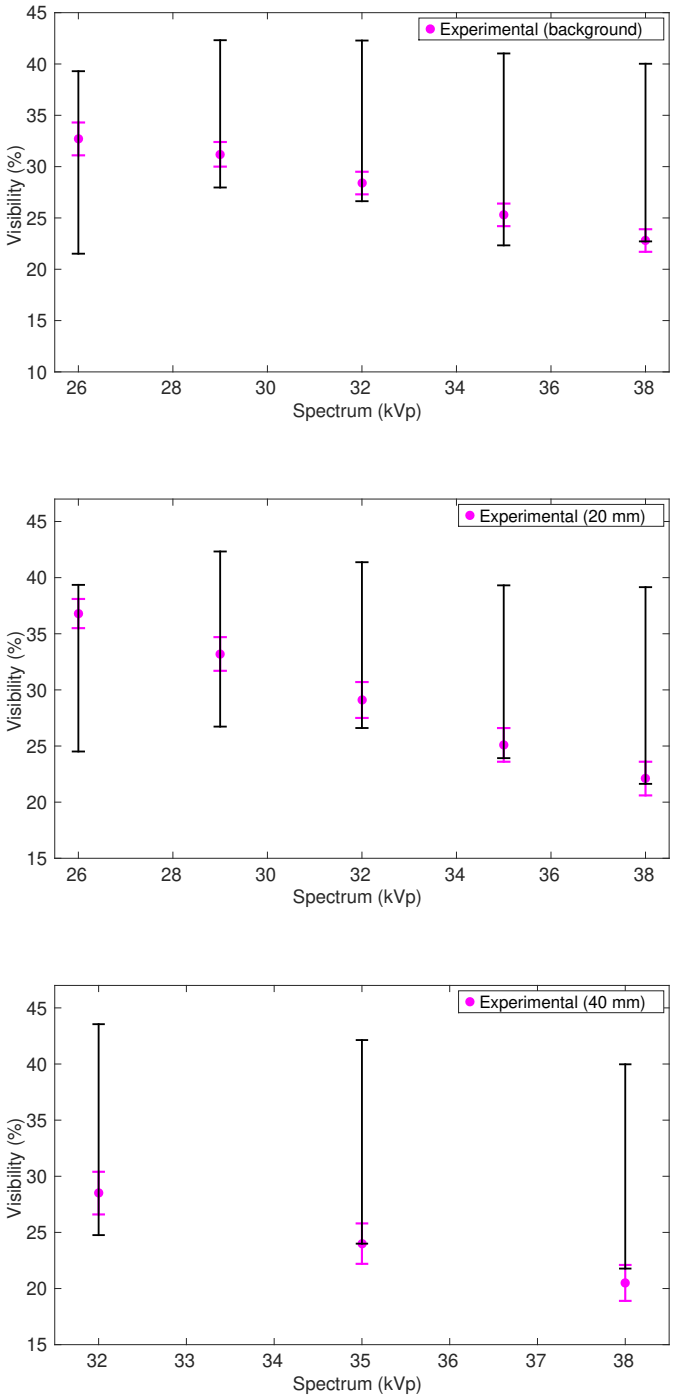

Fig. 5. Experimental (pink) and simulated (black bars) visibility values (%) for different Polycarbonate (PC) thicknesses and spectra. The standard deviation in the simulated values accounts for the potential grating height and duty cycle imperfections, while it refers to the noise in the experimental results.

Optics EXPRESS

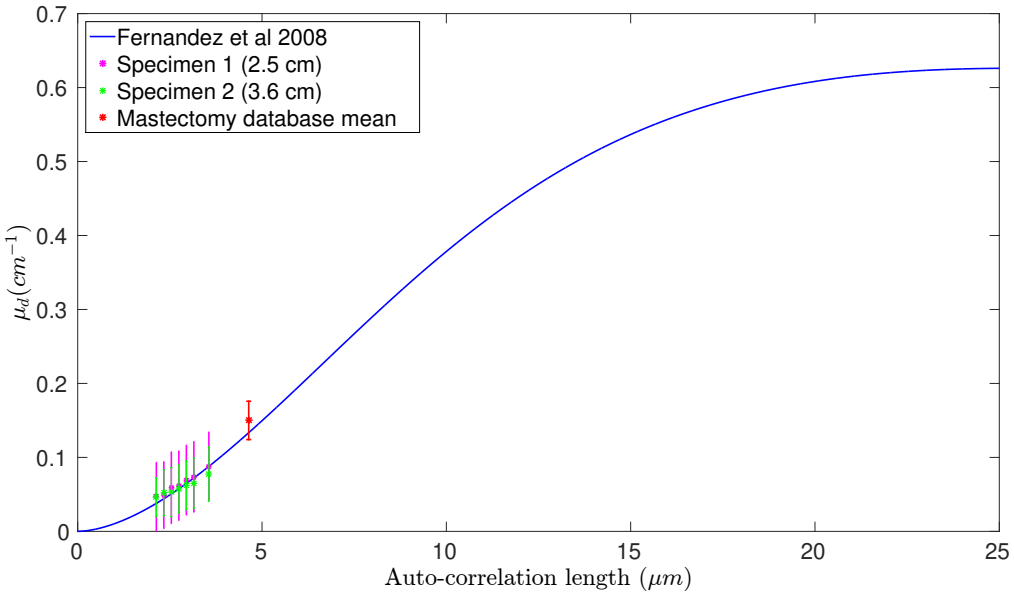

Fig. 6. Dark-field extinction coefficient (μ_d) for breast tissue as a function of the auto-correlation length. It can be seen that the detected visibility reduction changes with the auto-correlation length in a sigmoid manner for auto-correlation lengths below 20 μm, which suggests that the scatterers in the breast have roughly this size.

necessary to derive $G(\xi)$ for different types of microcalcifications (i.e. different shapes and clustering levels).

3.3. *Selection of the optimal GI parameters for the Philips Microdose Mammography setup*

The outcomes of our simulations are presented in Fig. 8. The optimal designs for each Talbot order with their corresponding sensitivity values are summarized in Table 2. As to the phase, it can be seen that the optimal values for all the Talbot orders are very close to one another, although it would be necessary to validate experimentally with breast samples what an increase of 0.2 electrons/(Å^3) means in terms of image quality. The third Talbot order appears to be the optimal for this metric, at a design energy of 23 keV and demanding a p_2 of 1.24 μm. This value is quite challenging from the fabrication point of view, so maybe the only realistic option would be to work at a first Talbot order, which does not require such a small pitch. Regarding dark-field, it can be seen that the best scenario is a 7th Talbot order. However, it demands a p_2 of 0.82 μm, which is even more challenging than the optimal for the phase.

The optimal design scenario is different for both metrics and this can be explained as follows. The measured phase shift, which has a direct dependency on the electron density gradient(Eqs. (4) and (6)), will increase as $\frac{p_2}{d}$ becomes smaller; since d is fixed in our case, the only way to decrease this ratio is by increasing the design energy so that the calculated p_2 decreases. However, the minimum detectable electron density also depends on the phase noise standard deviation that is determined by the background visibility, the visibility reduction, the flux and the sample transmission (Eq. (5)). The sample transmission and the flux are independent on the GI design scenario, so the differences in sensitivity behavior among various scenarios are due to the background visibility and visibility reduction trends. For the same inter-grating distance, as the Talbot order increases and p_2 decreases, the auto-correlation length increases and thus the

Optics EXPRESS

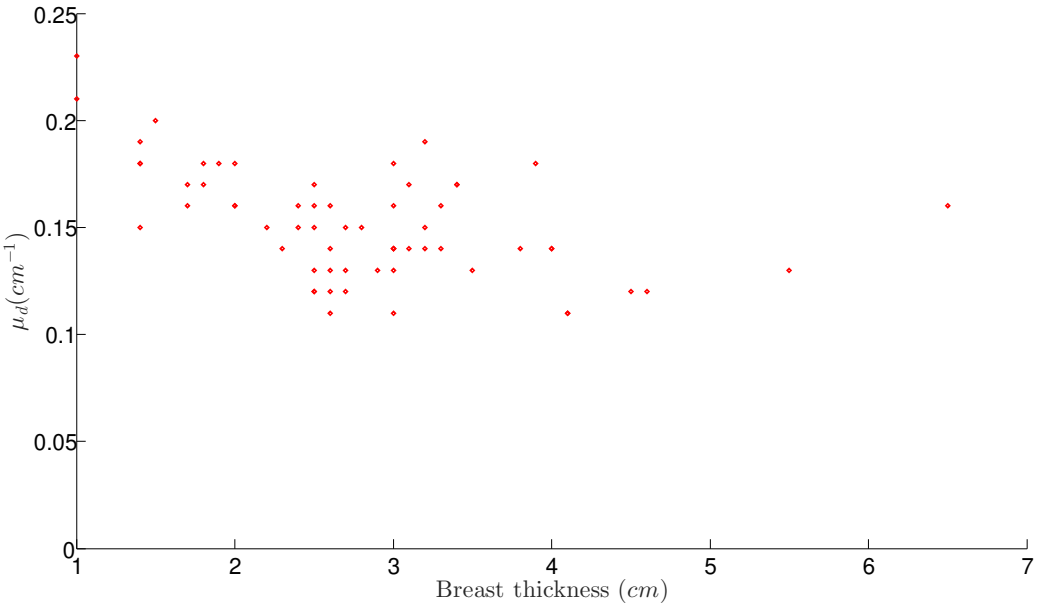

Fig. 7. Dark-field extinction coefficients (μ_d) for our fresh mastectomy database.

Table 2. Optimal scenarios for each Talbot order. For orders 1, 3 and 7, the optimal scenarios for both signals are the same, whereas for order 5 there are different optimal scenarios for phase[1] and dark field[2].

Talbot order	**Design energy (keV)**	p_2 **(μm)**	**Electron density (Å^{-3})**	**Dark-field (1/SNR)**
1	23	2.16	1.37	1.81
3	23	1.24	1.13	1.02
5^1	25	0.92	1.22	0.83
5^2	24	0.94	1.23	0.82
7	23	0.82	1.23	0.69

visibility reduction gets higher (Fig. 6), i.e. the phase noise standard deviation is larger. Taking all these factors into account, the optimal phase sensitivity scenario corresponds to one at which the best compromise between the geometric factor and the noise behavior is found.

In the dark-field signal case, the sensitivity metric is expressed as an SNR. The noise behavior of this signal follows the same dependency as the phase (Eqs. (5) and (13)). However, the signal itself also improves as the visibility reduction gets higher. Hence, the optimal dark-field scenario evidences this compromise between the signal and noise standard deviation trends by showing a low design energy and a high Talbot order, i.e. to make the auto-correlation length large, but not as large as to cause the noise to increase more than the signal.

To evidence why a higher Talbot order may be more useful in terms of dark-field sensitivity, the background and target breast visibility values for the optimal dark-field design energy are reported in Table 3. It is interesting to notice that the visibility difference between breast and background is minimal for the first Talbot order. As the latter increases, this difference and thus detectability in terms of dark-field, becomes larger.

The visibility decay produced as the Talbot order is increased is caused by the corresponding

Optics EXPRESS

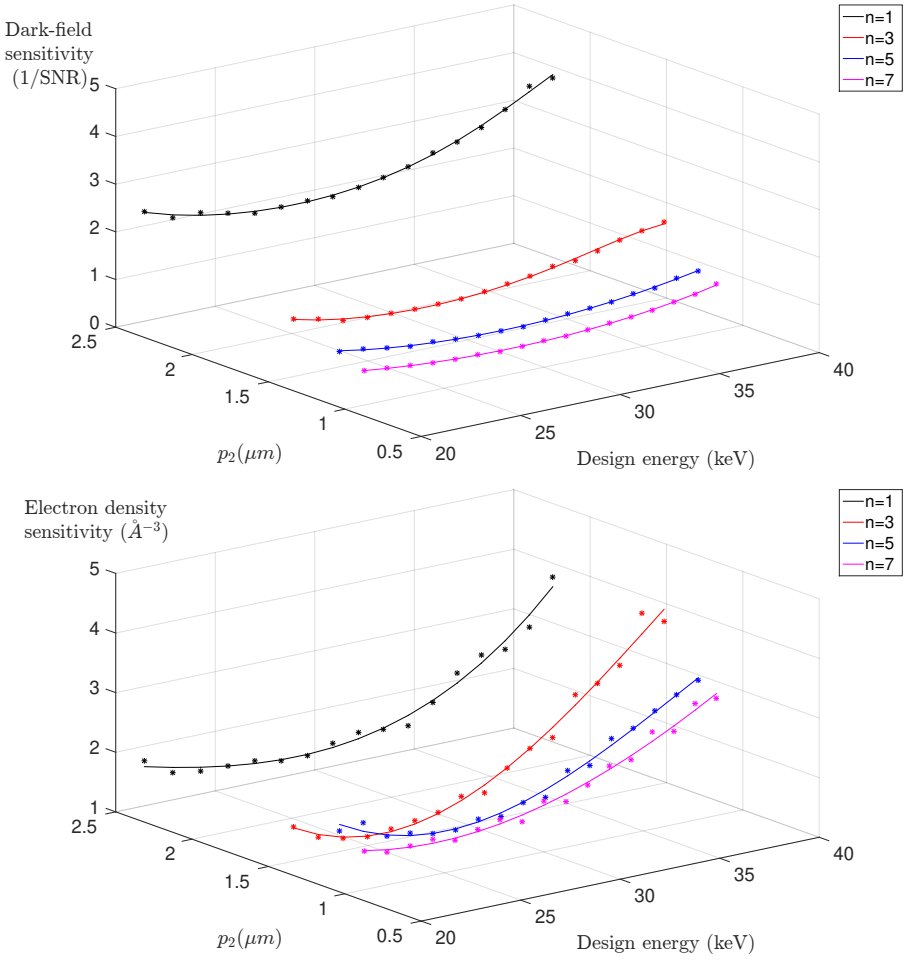

Fig. 8. Dark-field (top) and electron density (bottom) sensitivity vs. design energy for an inter-grating distance of 4 cm.

reduction in the spectral acceptance of the interferometer. This trend is confirmed by the formula derived in [29] for polychromatic visibility, as can be seen on the second column of Table 3. The difference in absolute values between the latter and our calculations is due to the fact that this formula assumes perfect spatial coherence and gratings, whereas our simulations take into account the finite focal spot size [34], limited grating heights, grating wafer thicknesses and detector stopping power.

The highest flux spectrum (i.e. 38 kVp) was used for our calculations because of the flux reduction caused by the introduced optical elements. It is also expected that this spectrum will yield the best sensitivity values. To verify this assumption, we computed the phase and dark-field sensitivities at the optimal design energy for each spectrum regarding the aforementioned constraints and the outcomes are presented in Table 4; it can be seen that there is a sensitivity gain by using the 38 kVp spectrum. However, although the SNR of the attenuation image is expected to be better by utilizing this spectrum, its soft tissue contrast might decrease for low breast thicknesses.

We measured the air kerma (K) on a Philips Microdose setup equipped with a G0 grating with a duty cycle of 0.5, a wafer thickness of 300 μm and a gold height of 30 μm. The measuring

Optics EXPRESS

Table 3. Visibility values (%) predicted by Thüring's formula and obtained from wave-optics simulations for the optimal dark-field sensitivity design energy (23 keV).

Talbot order	Background (Thuering's)	Background (simulated)	Breast (simulated)
1	49.9	36.1	33.3
3	35.2	27.1	21.8
5	32.6	23.2	16.2
7	34.5	23.5	14.8

Table 4. Phase and dark-field sensitivities for the optimal design scenario at each available Microdose spectrum.

Spectrum (kVp)	Minimum detectable electron density ($Å^{-3}$)	Dark-field sensitivity (1/SNR)
26	2.90	1.74
29	2.02	1.19
32	1.36	0.93
35	1.25	0.79
38	1.13	0.69

device was an ion chamber and it was placed on the breast support. At 38 kVp, we obtained a value of K=14.5 mGy and a half-value layer of 0.213 mm Al for an exposure time of 15 s. According to the European guidelines [35], the mean glandular dose (D) can be calculated as follows:

$$D = Kcgs, \tag{14}$$

where g is a factor corresponding to a glandularity of 50 %, c corrects for any difference in breast composition from 50 % glandularity, and s corrects for differences due to the choice of X-ray spectrum. The values g and c were calculated for our target breast by interpolation of the values reported in tables A5.1 and A5.2 [35], respectively. A resulting dose of 1.47 mGy was obtained. Since the maximum achievable value for this thickness (7 cm) is 3.1 mGy [35], the input flux could be more than doubled. An increase in flux would significantly contribute to improve the quality of the dark-field and differential phase contrast images.

One might think that an alternative scheme, allowing the use of longer inter-grating distances to obtain a higher sensitivity or larger p_2 values without making the GI less sensitive, is to position the breast between G1 and G2. We could make profit of the fact that the pre-collimator-detector separation is fixed and independent on the compression thickness for the selection of the inter-grating distance and place G1 onto the pre-collimator. However, this would imply that thinner breasts were placed further away from G1, which would cause an important sensitivity loss [36]. In addition, the reproducibility of the pre-collimator positions in all directions is very far from what is needed for an X-ray interferometer, so placing G1 right onto it would not be optimal. Therefore, using a sample-before-grating geometry is more convenient on this setup.

4. Conclusion

A GI-design optimization procedure employing the phase and dark-field sensitivities as figures of merit was developed, validated and used to calculate the optimal parameters for an interferometer that can be fitted into a Philips Microdose Mammography setup. The phase sensitivity was defined as the minimum detectable electron density gradient, whereas the dark-field sensitivity was defined as the target breast SNR. It was found that the optimal scenarios are the result of a compromise between the geometric factor, namely $\frac{d}{p_2}$, and the noise behavior of both signals,

Optics EXPRESS

which depends on the visibility reduction model, the sample transmission and the background visibility. For a fixed inter-grating distance of 4 cm, it was found that the optimal scenario for the phase is a third Talbot order GI with p_2 1.24 μm, whereas for dark field is a seventh Talbot order [37] with p_2 0.82 μm. Due to the extensive research on the contributions of the dark-field signal to mammography, it would be more logical to give preference to this signal and choose the latter scenario for implementation. An important contribution of this paper is a visibility reduction model for breast tissue, derived from measurements at different auto-correlation lengths.

Since the available inter-grating distance in this setup is so short, very small p_2 values are required for an improved sensitivity, mostly in the dark-field case. This fact significantly challenges the grating fabrication capabilities.

Future work will include measuring the dark-field extinction coefficients of different tissue types (microcalcifications, adipose and glandular), to be able to provide all the missing data for a clinically relevant system optimization, for example, in terms of dark field contrast-to-noise ratio.

In conclusion, we are now in the position to predict the performance of GI with respect to these metrics, so we can utilize our toolbox for future interferometer design tasks.

Funding

European Research Council (ERC) (ERC-2012-StG 310005-PhaseX); Swiss National Foundation (SNF)-Sinergia (CRSII2-154472 MedXPhase).

Acknowledgments

We thank Björn Cederström and Zsuzsanna Varga, who provided us with the set of simulated spectra and formalin-fixed samples, respectively.